



## Full length article

## Metastable high entropy alloys of TiZrHfTa with glass-like characteristics at low temperatures

Yanhui Zhang<sup>a,d,\*</sup>, Yunkai Zhou<sup>b</sup>, Li-Min Wang<sup>a</sup>, Stefano Sanvito<sup>c</sup><sup>a</sup> State Key Lab of Metastable Materials Science and Technology, and College of Materials Science and Engineering, Yanshan University, Qinhuangdao, Hebei 066004, China<sup>b</sup> Graduate department, Hebei Normal University of Science and Technology, Qinhuangdao, Hebei 066004, China<sup>c</sup> School of Physics and CRANN Institute, Trinity College, Dublin 2, Dublin, Ireland<sup>d</sup> Hebei Key Lab for Optimizing Metal Product Technology and Performance, Yanshan University, Qinhuangdao, Hebei 066004, China

## ARTICLE INFO

## Keywords:

Entropy  
Metastable phases  
Thermodynamics  
Density functional theory  
Cluster expansion

## ABSTRACT

Metastability engineering of high entropy alloys can widen the alloy-design window through the access of a potentially huge configuration space. At the same time, it has the great capacity to overcome the strength-ductility trade-off, where often one witnesses an actual performance improvement at low to cryogenic temperatures. An in-depth microscopic understanding of the underlying mechanism is now needed to drive the design effort. Here we investigate in detail the energetic, structural and chemical complexity of Ti–Zr–Hf–Ta system. The large configuration space with local chemical interaction heterogeneity is explored by a combination of structure-searching techniques and accurate energy models constructed by cluster expansion based on density functional theory data. We find that the potential energy landscape evolves towards displaying shallow mega-basins when decreasing the Ta content. This is accompanied by an expansion of the configurational density of states, which evolves to be clearly distinct from that of a homogeneous random solid-state solution. Furthermore, the energy-state variability and local configuration flexibility are identified from high throughput analysis of atomic structures and their energies. Such features remind closely what found in glass-like systems. This work suggests a theoretical connection between glass physics and metastability engineering of HEAs is quite promising.

## 1. Introduction

The general design concept of high-entropy alloys (HEAs) with multiple principal elements is that of enabling the formation of a single-phase random solid-state solution through the maximization of the configurational entropy at equiatomic composition [1–3]. Such simple idea, however, may not be the only enabler of multi-component alloys. In fact, the recent success in developing metastable alloys [4–6] has extended the range of the possible HEAs that can be synthesized to include compounds far away from both the thermodynamical equilibrium and equiatomic composition. Such strategy can even promote structural transformation between dual or multiple phases and, in general, it widens the alloy-design window via efficiently tailoring structural stability-related factors. Metastability engineering ultimately may offer an additional avenue to the design of HEAs with enhanced mechanical and functional properties [7]. For this reason it is important to investigate the physical and thermodynamic mechanisms behind metastability engineering in HEAs and to design a robust way to tune and access distinct metastable HEA states with substantial performance

improvements. Such understanding will enable the practical harnessing of the large configurational space available to HEAs.

Metastability engineering essentially consists in deliberately reducing the stability of the single-phase solid-state solution with the compositional tuning of the stacking-fault energy, a process that may result in an improved strength-ductility combination. However, one should also note that intricate microstructures and structure transformations have been observed in metastable HEAs, such as nanoscale segment de-trapping of dislocations, nano-twinning and local anti-phase boundaries [8], all effects that may contribute to their low temperature mechanical performances. This suggests that, more generally, in metastable HEAs the instability of the local atomic arrangement provides a fertile ground for the formation of complex microstructures. Such occurrence promotes transformation-induced plasticity, which in turn allows the HEAs to maintain high strength and ductility from room temperature down to cryogenic temperatures [9–13]. Furthermore, since chemical disorder and compositional fluctuations in HEAs

\* Corresponding author.

E-mail addresses: [yhzhang@ysu.edu.cn](mailto:yhzhang@ysu.edu.cn) (Y. Zhang), [zyk3908@hevtc.edu.cn](mailto:zyk3908@hevtc.edu.cn) (Y. Zhou), [limin\\_wang@ysu.edu.cn](mailto:limin_wang@ysu.edu.cn) (L.-M. Wang), [sanvitos@tcd.ie](mailto:sanvitos@tcd.ie) (S. Sanvito).

appear to determine energy dissipation and defects evolution, it has been discussed that metastable HEAs can be also designed to withstand radiation damage [14]. Theoretical calculations have been used to understand the relation between the stacking-fault energy and the chemical composition [15,16]. In order to realize a “metastability-engineering” strategy, a precise control of the local structures and the configurational entropy,  $S_{\text{conf}}$ , is essential, since both have a profound impact on the thermodynamic stability of the HEAs, as well as on the overall shape of their phase diagram [17]. Unfortunately, the extremely large compositional space of HEAs poses a serious challenge for computational and experimental materials science, making the tuning of the configurational space and of  $S_{\text{conf}}$  of multi-component systems very challenging.

In general, as the number of species forming a compound grows, the Gibbs free energy will be dominated by the entropic contribution, which will determine the phase stability regardless of the possible enthalpy. An analysis over the large AFLOWLIB.org database [18] reveals that four species corresponds to the crossover threshold of the entropic contribution, thus setting the boundary between possible ordered and disordered phases [19]. For HEAs, one can then compute the configurational entropy of mixing from the ideal solid-solution model, a strategy that allows one to formulate simple stability descriptors able to rank possible compositions according to their forming ability [20]. However, given that many HEAs are known to exhibit phase separation and structural complexity at low temperature, it was later recognized that the simple ideal solid-solution model only provides an upper bound to the configurational entropy at high temperature. The computational strategy then consists in combining cluster expansion (CE) Hamiltonian and Monte Carlo simulations [21,22], which together have enough throughput and precision. Notably, however, this may not be the final solution to the problem of predicting phase stability of HEAs, since an excess entropy of mixing (the difference between the actual mixing entropy and the ideal solid-solution entropy) up to  $0.9R$ , has been measured in NiCoFeCr alloys [23].

Here we investigate the origin of the metastability of the prototype HEA system, Ti–Zr–Hf–Ta, by using a combination of density functional theory (DFT), machine learning and cluster expansion (CE) [24]. These are used to evaluate the electronic structure and energetics of special quasi-random structures (SQSs) [25] and to evaluate the potential energy landscape (PEL) across different phases. Furthermore, by using non-equivalent supercell enumeration [26] and Wang-Landau sampling (WL) [27] we compute the configurational density of states (cDOS), the configurational entropy and the distribution of formation energies with composition variation. This analysis returns us a picture where ideal solid-state solutions in the Ti–Zr–Hf–Ta system can exist only at high temperature, while the *bcc* phase is metastable at low temperature. The glass-like PELs and the predicted wide fluctuations in the chemical and compositional local order further suggest that martensitic transitions triggered by mechanical load will be possible.

## 2. Calculation methods

### 2.1. Construction of the SQS supercells and potential energy landscapes

Equiatomic *bcc* TiZrHfTa is modeled by constructing supercells containing 36, 48, 72, 96 and 128 atoms. These are obtained as a  $2 \times 3 \times 3$  (36 atoms),  $4 \times 3 \times 3$  (72 atoms),  $4 \times 4 \times 3$  (96 atoms) and  $4 \times 4 \times 4$  (128 atoms) expansion of the *bcc* 2-atom unit cell. The only exception is the 48-atom supercell, which is constructed as a  $3 \times 2 \times 2$  expansion of the 4-atom *bcc* cell, whose lattices vectors are along the  $[001]$ ,  $[110]$  and  $[110]$  directions. In order to simulate structures resembling a uniform solid-state solution the special quasi-random structures (SQSs) method [25] is used to decorate the supercells. In this the pair probability of the first few nearest-neighbor shell is optimized to be close to that of an ideal mixing state.

The pseudo-binary alloys TiZrHf $_{1-x}$ Ta $_x$  are modeled by using three sets of SQSs containing, respectively 36, 48 and 72 atoms. Their detailed composition can be found in Figs. 1 and S6. The cohesive energy across a mesh of lattice parameters,  $a$ , and  $c/a$  ratios is calculated by using the density functional theory (DFT) code VASP [28] at 0 K (see later DFT details). A total of 13802 SQS cells are constructed to mesh out the PEL profiles. The variation of the PEL profiles with the lattice parameters is much more significant than the rather tight energy variation obtained by changing the atomic positions due to atomic relaxation. Note that the computational load of DFT calculations for 13802 supercells is quite enormous. Therefore, no atomic relaxations are performed for PEL exploration using SQS cells.

### 2.2. Structural enumeration and low-energy search

Information about the configuration and energy distributions of metastable HEAs are obtained by constructing simulation supercells with three different structure-searching techniques, namely non-equivalent supercell enumeration (Enum) [26], ground state searching (GSS) [29,30] and Wang-Landau (WL) sampling (WL) [27]. These are applied to the equiatomic alloys, *hcp* ZrHf, *bcc* ZrTa (BCC) and *bcc* TiZrHfTa. Enum is an efficient method to generate derivative superstructures for an arbitrary parent structure and it is used here to generate supercells containing up to 14 atoms. In contrast, GSS structures are obtained by listing all the possible chemical arrangements in cells including up to 20 atoms, while 192-atoms WL structures have been sampled by the flat-histogram method. The number of structures found with the different procedures is listed in Table 1. Their formation energies are calculated as

$$\Delta E_f = \frac{E_{\text{tot}} - \sum n_i \cdot E_i}{\sum n_i}, \quad (1)$$

where  $n_i$  is the number of atoms of the  $i$ th specie in the cell,  $E_i$  is the total energy of the corresponding elemental structure and  $E_{\text{tot}}$  is the total energy of the mixture. Here energy data for the Enum structures are provided by DFT calculations with full structure relaxation, while those of the GSS and WL prototypes are obtained from the cluster expansion (CE) with a fix lattice.

### 2.3. Construction of the cluster expansion models

The energy calculation of the substantial number of GSS- and WL-generated structures is beyond the DFT throughput and thus requires the use of an accurate and efficient Hamiltonian. This can be obtained with the CE method, which implements a practical lattice-gas-type model and enables both a comprehensive sampling of the many-dimensional configuration space and the effective mapping of the potential energy surface of multi-component systems. In the CE framework a parametrized Hamiltonian is employed to calculate the energy of an arbitrary configuration  $\sigma$ . Such Hamiltonian has the form of a generalized Heisenberg model

$$\begin{aligned} E^{CE}(\sigma) &= J_0 + \sum_i J_i \sigma_i + \sum_{i,j} J_{ij} \sigma_i \sigma_j + \sum_{i,j,k} J_{ijk} \sigma_i \sigma_j \sigma_k + \dots \\ &= J_0 + \sum_{\alpha} \langle \Pi_{\alpha'}(\sigma) \rangle m_{\alpha} J_{\alpha} = \Pi J, \end{aligned} \quad (2)$$

where  $\sigma_i$  represents the occupations of the  $i$ th atomic specie and the  $J$ 's are the effective coefficients of interaction of the clusters. The Hamiltonian thus contains multi-body interaction terms of different order so that  $\alpha = [\sigma_1, \sigma_2, \dots, \sigma_i]$  corresponds to a cluster with the multiplicity  $m_{\alpha}$ . The  $\langle \dots \rangle_{\alpha}$  bracket indicates that the average is performed over the basis functions for all clusters that are symmetry equivalent to  $\alpha$ .

Due to its high-speed and applicability over a wide range of configurations and compositions, CE is useful for performing ground-state searches and Monte-Carlo simulations. Here, the integrated cluster expansion toolkit (ICET) [24] is used to build the CE Hamiltonian for *hcp* ZrHf, *bcc* ZrTa and *bcc* TiZrHfTa. The effective coefficients of

interaction are fitted to a set DFT reference energies obtained for a library, including elementary, binary, ternary and quaternary alloys with a wide composition range. The structures are determined with the structure-enumeration feature of ICET, which provides symmetry inequivalent prototypes with a large spectrum of energy distribution. The as-generated prototypes library is first filtered to remove those structures with volumetric strain larger than 10% and/or atomic displacement larger than 0.5 Å, a procedure that improves the accuracy of the lattice model. In total the reference dataset contains 176, 147 and 631 distinctive structures, respectively for the *hcp* Zr–Hf, *bcc* Zr–Ta and *bcc* Ti–Zr–Hf–Ta systems.

In practice, the accuracy of a CE Hamiltonian can be assessed with the so-called cross-validation score, defined as

$$CV = \sqrt{\frac{1}{n} \sum_i (E_i^{\text{CE}} - E_i^{\text{DFT}})^2}, \quad (3)$$

namely the square-root of the mean-square distance between the CE energy prediction,  $E_i^{\text{CE}}$ , and the DFT reference,  $E_i^{\text{DFT}}$ , over the  $n$ -element dataset. The accuracy of a CE can be systematically improved by including clusters of progressively higher order. Here the cluster pools have been prepared by considering zerolets, singlets, pairs, triplets and quadruplets. The cut-off radii are chosen to be  $2.0a_0$ ,  $1.7a_0$  and  $1.4a_0$  ( $a_0$  is the lattice parameter of the parent lattice) for pairs, triplets and quadruplets, respectively. Note that we include up to 227 clusters for the Ti–Zr–Hf–Ta *bcc* system. We carefully monitor the possibility of overfitting by using the machine-learning scheme of least absolute shrinkage and selection operation (LASSO). This consists in regularizing the fit by mean of a regularization term with hyper-parameter of  $\beta$

$$J_{\text{optimal}} = \text{argmin} \|IIJ - E^{\text{DFT}}\|_2^2 + \beta \|J\|. \quad (4)$$

After testing various combinations, we have decided to employ 11, 17 and 20 clusters, respectively for the *hcp* Zr–Hf, *bcc* Zr–Ta and *bcc* Ti–Zr–Hf–Ta systems. These are the most representative clusters for the total energy evaluation. During the optimization process of the  $J$ 's the reference datasets are split into training and testing set with a 4:1 ratio by the shuffle split iterator. The obtained learning curves are plotted in Fig. S1 panels (a), (b) and (c) (see SI), while the predicted formation energy are compared with those computed with DFT (training and test sets) in Fig. S2. Finally, the optimized  $J$ 's are shown in Figs. S3, S4 and S5, respectively for the *hcp* Zr–Hf, *bcc* Zr–Ta and *bcc* Ti–Zr–Hf–Ta systems. The  $CV$  scores obtained are 0.3 meV/atom, 8.0 meV/atom and 15.0 meV/atom, respectively for *hcp* Zr–Hf, *bcc* Zr–Ta and *bcc* Ti–Zr–Hf–Ta. The figure shows that there is good alignment of the data along the parity line with coefficients coefficient of determination,  $R^2$ , 0.96 (0.90), 0.95 (0.88) and 0.95 (0.94) over the training (test) set. The maximum differences between the CE and DFT energies are below 1 meV/atom, 25 meV/atom and 50 meV/atom. With these results at hand we can conclude that the CE models can reach a very satisfactory accuracy in the energy prediction of the various alloy systems.

#### 2.4. Wang-Landau sampling

The Wang-Landau (WL) random walk [27] is an accurate and efficient algorithm to directly calculate the configuration density of state (cDOS) for complex systems with a rough energy landscape. The scheme provides two great advantages over conventional Monte Carlo simulations. On the one hand, WL sampling overcomes the tunneling barriers for both 1st- and 2nd-order phase transitions, since the random walk does not depend on the temperature. Thereby, it allows us to sample the configuration space with much less effort by directly calculating the cDOS and makes the study of HEAs with both random and locally ordered structures feasible. On the other hand, the free energy and the configurational entropy can be readily calculated. In fact, after the WL sampling scheme has generated an accurate cDOS,  $g(E)$ , the partition function can be obtained as

$$Z = \sum_E g(E) e^{-\beta E}. \quad (5)$$

Then, the free energy  $F$ , the internal energy  $U$ , the configurational entropy  $S_{\text{conf}}$  and the specific heat  $C_v$  due to configurational variations can be separately obtained, as

$$F(T) = -k_B T \ln(Z), \quad (6)$$

$$U(T) = \langle E \rangle_T = \frac{\sum_E E g(E) e^{-\beta E}}{\sum_E g(E) e^{-\beta E}}, \quad (7)$$

$$S_{\text{conf}}(T) = \frac{U(T) - F(T)}{T}, \quad (8)$$

$$C_v(T) = \frac{\langle E^2 \rangle_T - \langle E \rangle_T^2}{T^2} = \frac{dS_{\text{conf}}(T)}{d \ln T}. \quad (9)$$

In addition, the degree of deviation of the configurational entropy from the ideal-mixing entropy,  $S^{\text{id}}$ , can be estimated by using the following dimensionless quantity

$$Q(T) = 1 - \frac{S_{\text{conf}}(T)}{S^{\text{id}}}. \quad (10)$$

#### 2.5. Density functional theory calculations

DFT calculations have been performed by using the plane-wave basis-projector augmented-wave method (PAW) [31] as implemented in the VASP [28] code. For the transition metals Ti, Zr, Hf and Ta, we adopt the generalized gradient approximation to the exchange–correlation functional as proposed by Perdew, Burke and Ernzerhof (PBE) [32]. In addition semi-core states are treated as valence (Ti<sub>sv</sub>, Zr<sub>sv</sub> and Hf<sub>sv</sub> in the VASP distribution). The Brillouin zone is sampled with a  $k$ -point grid equivalent to a  $20 \times 20 \times 20$ -mesh for the primitive *bcc* unit cell and the plane wave cutoff energy is set to 520 eV. Both the atomic positions and the cell parameters are relaxed until the residual stress is less than 0.01 GPa by carrying out first-order Methfessel–Paxton smearing with a width of 0.16 eV.

### 3. Results

#### 3.1. Low-temperature energy landscape

Experimental evidence shows that Ti–Zr–Hf–Ta alloys with low Ta content are characterized by the presence of two phases, *bcc* and *hcp*, and of a stress-induced martensitic transformation [6,7]. In order to evaluate the energetics of the different phases we first compute the PELs. These provide a good understanding of the relative phase stability at low temperature, where entropic effects are less important. The PELs are obtained from the DFT cohesive energy of SQS cells as a function of the lattice parameter,  $a$ , and the  $c/a$  ratio, for different atomic compositions.

In Fig. 1, panels (a) through (c), we show such PEL profiles for (TiZrHf)<sub>1-x</sub>Ta<sub>x</sub> at  $x = 0.25, 0.167$  and  $0.138$ , obtained with a 32-atom SQS cell. One can clearly note a double-funnel structure appearing at a Ta content of 0.250 and 0.167. The two deep energy minima correspond to the *bcc* and the *hcp* phase, respectively, and they are separated by a high energy barrier. This suggests that the thermodynamically stable *bcc* phase at high temperature can be easily trapped at low temperature, becoming long-living metastable. As a consequence the martensitic transition *bcc* → *hcp* is strongly suppressed at a relatively high Ta content. Then, as the Ta fraction is reduced the cohesive energy of both phases gets smaller (in absolute value) and, most importantly, the PEL profile becomes more shallow. This can be clearly seen in Fig. 1(c), where the two energy minima are still visible at  $x = 0.138$ , although they appear much broader than those computed at higher  $x$ . As such, the PEL at low Ta concentration resembles that of amorphous glass materials with shallow and flatten meta-basins instead of deep and sharp minima [33] for typical crystalline materials. This feature suggests the possibility to reshape a metastable HEA locally with structural transformation and the evolution of intricate local microstructures, or even glass transition during non-equilibrium processing.



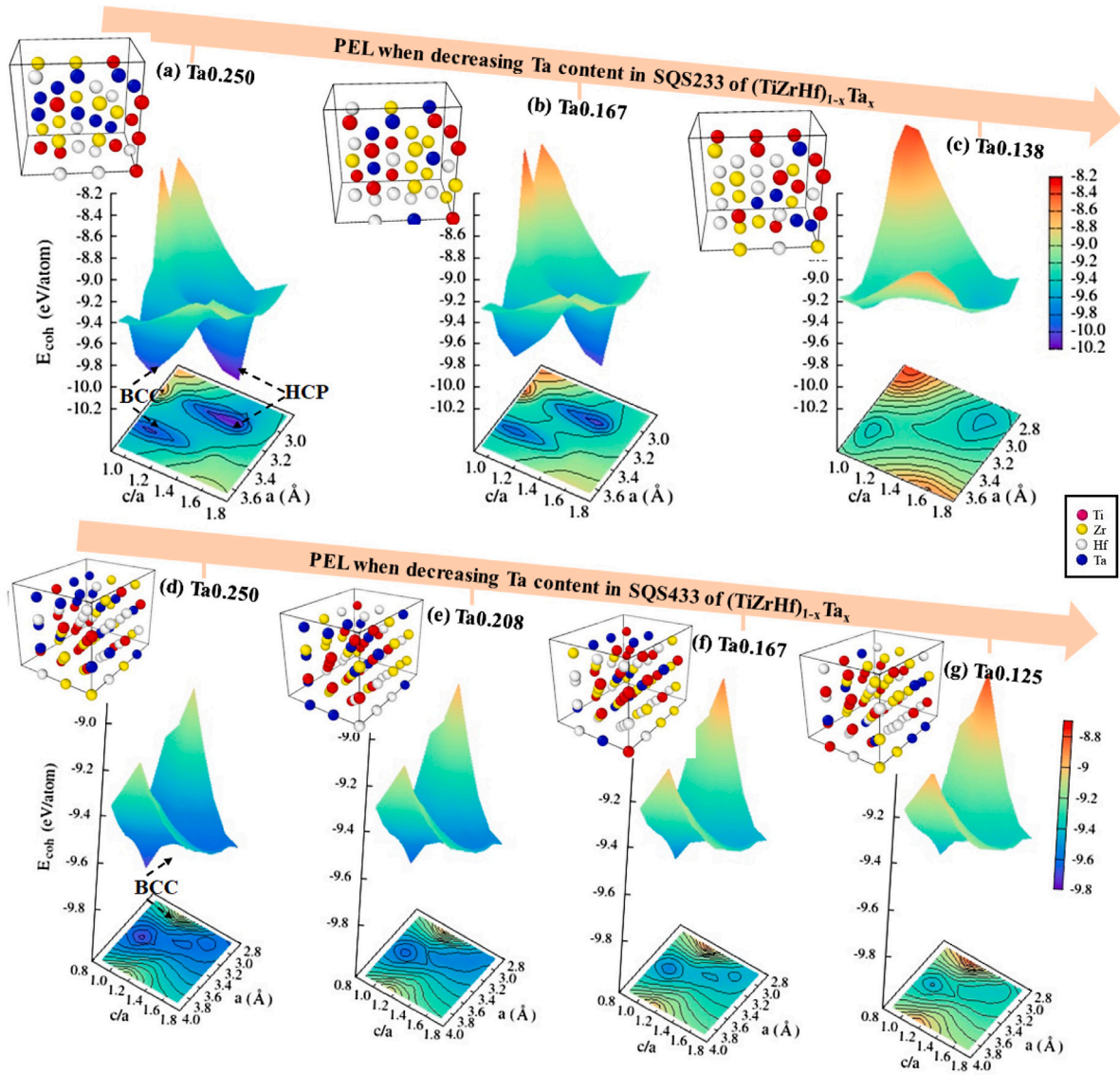


**Fig. 1.** The potential energy landscapes (PELs) of  $(\text{TiZrHf})_{1-x}\text{Ta}_x$  are presented as 3D and 2D projections of the cohesive energy,  $E_{\text{coh}}$  (eV/atom), as a function of the lattice constant,  $a$ , and the  $c/a$  ratio. Panels (a), (b) and (c) are obtained with a 36-atom-SQS cell at a Ta content  $x = 0.250, 0.167$  and  $0.138$ , respectively. Panels (d), (e), (f) and (g) are for a 72-atom-SQS cell with  $x = 0.250, 0.208, 0.167$  and  $0.125$ , respectively.

In the computed PELs the meta-basins contain several minimum crystalline states, which overall occupy a large hyper-volume of the configuration space, in particular when one assumes fluctuations in the local chemistry. If external mechanical load is applied, flexible variations of the local atomic configuration can then be easily accommodated. These may result in either remaining in the same meta-basin or in escaping in an adjacent one. The martensitic transformation between the *bcc* and *hcp* phase can take place when escaping occurs. If, instead, the compound remains within the same shallow *bcc* meta-basin, one has to expect a broad variation of the local atomic configuration, in particular if the Ta distribution is not uniform. The possibility of extended lattice adjustments under mechanical load, as suggested from the calculated PELs, may offer a possible explanation for the formation of the wide phase boundary between the *bcc* and *hcp* phases, as observed by *in-situ* high-resolution tunneling electron microscopy measurements [6]. In summary, our calculated PELs clearly demonstrate that the origin of the flexible structural transformation and complex microstructure of metastable Ti–Zr–Hf–Ta HEAs can be traced back to the shallow glass-like shape observed at low Ta contents.

An interesting feature observed when calculating the PELs is that the energy profile as a function of the Ta content varies for the *hcp*

phase, but remains unchanged for the *bcc* phase with the SQS cells used. This can be appreciated in Fig. 1, panels (d), (e), (f) and (g), where we present data for 72-atom cells at  $x = 0.25, 0.208, 0.167$  and  $0.125$ , respectively, and in Fig. S6 (see supplementary information — SI), where we show results for 48-atom cells at  $x = 0.25, 0.188$  and  $0.125$ . In general, we find that the picture at low Ta content is quite similar in all cases with the *bcc* and *hcp* meta-basin fusing together in a glass-like PEL structure. In contrast, for  $x > 0.2$  the *bcc* minimum appears always well defined, while the broadening of the *hcp* one depends on the size of the SQS cells used. This makes it difficult to provide a fully quantitative assessment of the structure transformation condition. One guess for the reason behind is the variation of the energy states with the local chemistry heterogeneity or local atomic distributions.

To validate this idea, finite size tests of SQS energies are performed and the energy states are checked by employing different structure-searching techniques. Since the energy states of SQS cells are affected by both the distributions of various species within the cells and the cell sizes, the cohesive energies, of equiatomic TiZrHfTa are calculated using multiple SQS cells of different sizes, 36, 48, 72, 96 and 128 atoms, respectively. These results are presented in the SI, Fig. S7, for the *bcc*

**Table 1**

Gaussian fitting parameters for the formation-energy distributions presented in Fig. 2. Here we report the Gaussian center,  $\mu$ , the standard deviation,  $\sigma$ , and the total number of alloys configurations constructed,  $N_{\text{conf}}$ . Prototype structures are generated with GSS, Enum and WL techniques (details in Sections of 2.2 and 2.4).

	$\mu$ (meV/atom)			$\sigma$ (meV/atom)			$N_{\text{conf}}$		
	GSS	Enum	WL	GSS	Enum	WL	GSS	Enum	WL
<i>hcp</i> -ZrHf	0.71	0.78	1.11	0.70	1.26	1.67	61 965	58	2791
<i>bcc</i> -ZrTa	120.25	121.86	124.32	14.67	29.35	40.43	99 469	54	105 777
<i>bcc</i> -TiZrHfTa	46.55	60.34	56.32	11.21	22.97	26.79	2423	76	67 171

structure. As expected, the energy converges very fast with growing the SQS cell sizes. At the same time, the energy fluctuations are more pronounced for smaller SQS cells, with a distribution width of about 9 meV/atom for 36-atom cells, which reduces to about 3 meV/atom for 128-atom cells. Such distributions are, in general, rather tight, suggesting that already small cells are representative of random structures. Although, different quantities may converge differently with respect to the SQS-cell size [34], we conclude that SQS cells with moderate sizes are sufficient for random solid solution modeling with degenerate energy states. We also observe that, if some level of local order is found, as the one intrinsically present in small SQS cells, then the case is too complex to be modeled using SQS cells. Since the energy-state variability and the local chemistry heterogeneity behind the local atomic ordering and the structure transition is related to how the supercells are decorated. This makes the SQS method not feasible for structure searching of non-degenerate energy states within the huge configuration space.

In order to better understand the energy distributions and chemistry homogeneity/heterogeneity of alloys with different stability, we analyze in detail the case of the stable *hcp* ZrHf solid-state solution, the unstable *bcc* ZrTa mixture and the metastable *bcc* TiZrHfTa. The atomic configurations of the selected compositions are generated by employing three different structure-searching techniques, namely (1) enumerating non-equivalent supercells (Enum) [26], (2) low-energy structure exploration by ground-state searching (GSS) [29,30] and (3) Wang-Landau (WL) [27] sampling (see method section). Histograms of the  $\Delta E_f$  distributions are presented in Fig. 2, where we also show their corresponding Gaussian fits, with the fitting parameters reported in Table 1. Let us start from *hcp* ZrHf, for which the stability of the solid-state solution is confirmed by a distribution with extremely small average,  $\sim 1$  meV/atom, and standard deviation,  $\sigma$ , also  $\sim 1$  meV/atom. This means that the ZrHf solid-state solution is almost iso-enthalpic with the individual Zr and Hf phases, while the entropy is maximized (using the entropy-forming-ability descriptor,  $\sigma$  is a proxy for the entropy [20]). In contrast,  $\Delta E_f$  of the unstable *bcc* ZrTa mixture is centered at around 122 meV/atom with standard deviation of about 30 meV/atom (note that these values change depending on the sampling technique used, see Table 1). Finally, as expected the metastable *bcc* TiZrHfTa alloy sits in between the previous two cases with an average  $\Delta E_f$  of 54 meV/atom and a standard deviation of  $\sim 20$  meV/atom. In general, for metastable multi-component alloys one should expect a relatively wide energy distribution over the configuration space, a feature that stems from the broadening of the PEL mega-basins as the local stoichiometry fluctuates. This behavior is sharply different from what found in a solid-state solution that, in contrast, presents a highly degenerate energy distribution.

Interestingly, the inclusion of atomic relaxation did not change the distribution of formation energies, as shown in Fig. 2. The enumerated structures are fully DFT relaxed, including atomic relaxation. Their formation energies at equimolar compositions are compared with those of GSS and WL structures, whose energies are calculated using CE with a fix lattice. All three kinds of energy exploration methods show similar energy distributions. That says that the formation-energy distributions obtained with or without the inclusion of atomic relaxation deliver the same story, which makes the metastable TiZrHfTa distinguished from a random solid solution.

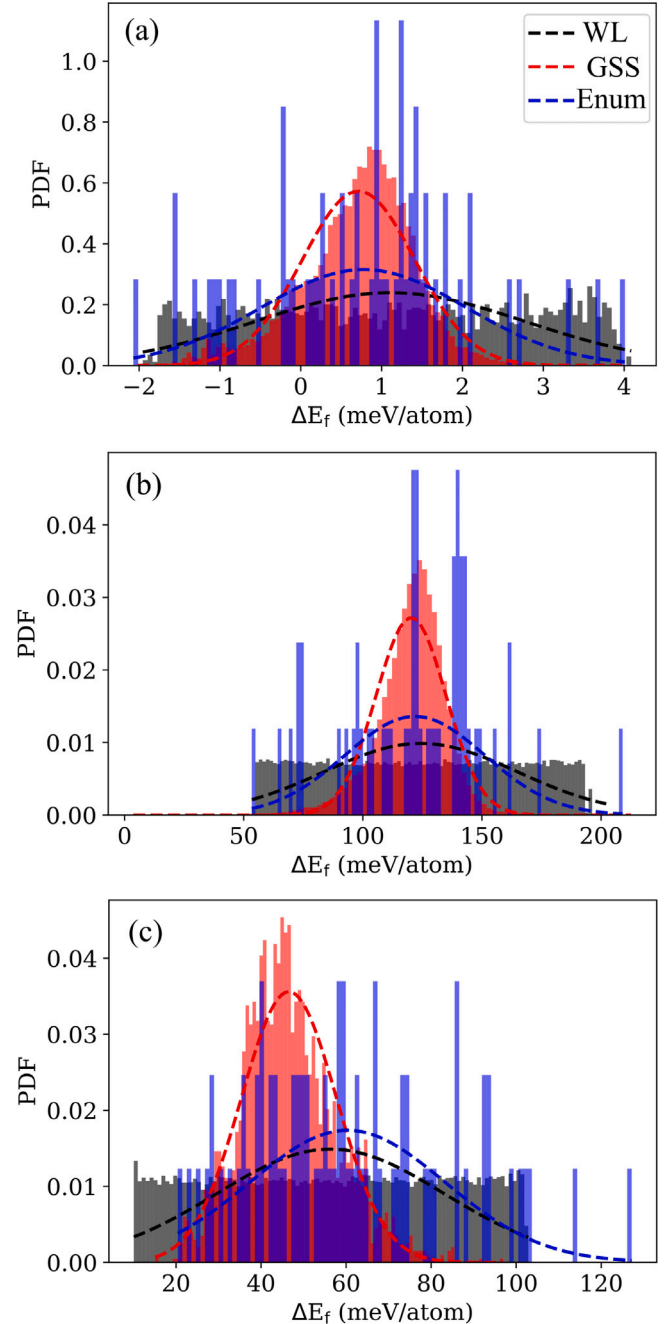


**Fig. 2.** Distribution of the formation energy,  $\Delta E_f$  (meV/atom), for the equiatomic alloys, (a) *hcp* ZrHf, (b) *bcc* ZrTa and (c) *bcc* TiZrHfTa. The calculated histograms are fitted with Gaussians (dashed lines). For each alloys, configurations are built using three different sampling techniques: enumerating non-equivalent supercells (Enum), ground-state search (GSS) and Wang-Landau (WL) sampling. The energy data for the Enum method are from DFT, while those for GSS and WL are from the cluster expansion for  $\text{Zr}_{1-x}\text{Hf}_x$ ,  $\text{Zr}_{1-x}\text{Ta}_x$  and  $\text{Ti}_x\text{Zr}_y\text{Hf}_z\text{Ta}_k$ , respectively.

### 3.2. Local chemistry inhomogeneity

A deeper insight into the metastability of HEAs can be obtained by simulating the energetic variations within the chemical configuration space. This is realized by taking advantage of the Wang-Landau (WL) sampling algorithm, whose energies can be provided by the cluster-expansion [35]. The combined scheme, thus, offers an efficient description of the variation of the energy with configurations, namely with the distribution of the different species over the parent lattice. Note that the WL method can efficiently sample the huge configuration space available to metastable HEAs with rugged PELs, since it can overcome large potential barriers [27]. By computing an accurate cDOS, we can then obtain the configurational entropy,  $S_{\text{conf}}$  and the specific heat,  $C_v$  (see Method section). Our results suggest that the wide energy window of metastable HEAs is the result of the disturbance of the local structure homogeneity related to the composition fluctuations.

The cDOS, obtained by WL sampling and CE is presented in Fig. 3(a) for equiatomic *hcp* ZrHf, *bcc* ZrTa, *bcc* ZrHfTa and *bcc* TiZrHfTa. The stable ZrHf solid-state solution and the unstable ZrTa mixture have been chosen as reference systems to be compared with the other two, whose nature is more uncertain. As expected stable ZrHf and unstable ZrTa present, respectively, the narrowest and the broadest cDOS distribution, reflecting their relative stability. Interestingly, when adding Hf and Ti to the *bcc* ZrTa phase, going to equiatomic ZrHfTa and TiZrHfTa, the cDOS shrinks while the center of the distribution moves to lower  $\Delta E_f$ , despite the fact that their global configuration space becomes considerably larger. This behavior somehow intermediate between that of solid-state solutions and unstable alloys is associated to the metastability. However, this cannot work as an exact indicator of the extent of metastability. Since the structural transition path and the related energy barriers among various energy minimums vary with variables adopted within the structural space.

Next, the computed cDOS are used to calculate the configurational entropy,  $S_{\text{conf}}$ , following the definitions provided in Eq. (5) through Eq. (8). These are plotted in Fig. 3(b) as a function of the temperature. It is shown that the absolute values of the configurational entropy, scaled by the gas constant of  $R$ , increase largely when increasing the number of components. With the only exception of *hcp* ZrHf,  $S_{\text{conf}}$  of all the alloys deviates significantly from the ideal-mixing-entropy limit (dashed lines), a deviation that is quantified in Fig. 3(d). Reflecting the behavior observed for the cDOSs, we note that for the metastable *bcc* ZrHfTa and TiZrHfTa alloys the deviation of  $S_{\text{conf}}$  from the ideal-mixing limit is intermediate between that of *hcp* ZrHf, which shows little deviation, and that of *bcc* ZrTa, which deviates at almost any temperature. In fact, for *bcc* ZrHfTa and TiZrHfTa alloys the deviation is significant only below 600 K. This behavior suggests the possible presence of chemical short-range order in those metastable alloys [36], as we will discuss further below. Furthermore, comparing the configurational with the vibrational contribution to the excess entropy of mixing (see Fig.S11 in SI), we can conclude that the configurational entropy plays a significant role and cannot be ignored, as it can explain demixing or structural transformations [36].

Finally, we turn our attention to the configurational specific heat,  $C_v$ , which is plotted as a function of temperature in Fig. 3(c). In contrast to the stable *hcp* ZrHf alloy, whose  $C_v$  remains little temperature dependent and small across the entire range investigated, both unstable and metastable alloys display a peak structure. For instance, the metastable equiatomic *bcc* TiZrHfTa has a dominant peak at about 150 K and a broader satellite above 400 K. In all cases  $C_v$  tends to vanish at high temperature, where the configurational entropy approaches the ideal-mixing limit and where the solid-state solution becomes entropically stabilized. A peak in the configurational specific heat corresponds to a temperature, where the fluctuations in the local configurations are maximized [37]. We attribute the origin of such fluctuations to some level of chemical composition order, an hypothesis that can be verified

by investigating the temperature-dependent short-range order (SRO) parameters [38].

These are computed from the trajectories of the WL sampling process and presented in Fig. 4(a) for the Zr–Hf pairs and in Fig. 4(b) for the Zr–Ta ones. The stable *hcp* ZrHf solid-state solution has a vanishingly small SRO value at any temperature, indicating the absence of chemical order and the homogeneity of the random-mixing state. In contrast, the SRO parameters for both the metastable ZrHfTa and TiZrHfTa alloys (and for the unstable ZrTa) all deviate significant from zero. Interestingly, while that associated to the Zr–Hf pairs does not display any significant structure as a function of temperature, the one related to the Zr–Ta pairs is maximized at low temperature, in the same region where the specific heat shows the peak structure. This seems to suggest that partial order of the Zr–Ta atoms is at the origin of the temperature profile of the specific heat.

### 3.3. Composition/configuration-dependent energetics of *bcc* (TiZrHf)<sub>1-x</sub>Ta<sub>x</sub>

We now perform the same analysis of the previous section for *bcc* (TiZrHf)<sub>1-x</sub>Ta<sub>x</sub>, which is treated here as a pseudo-binary system, namely Ti, Zr and Hf remains always in equal atomic proportions. The Ta-dependent cDOS and the degree of deviation of  $S_{\text{conf}}$  from the ideal-mixing entropy are plotted in Fig. 5(a) and (b), respectively. Their accuracy test are shown in Figs. S8, S9 and S10 in the SI. It is expected that the (TiZrHf)<sub>1-x</sub>Ta<sub>x</sub> alloys show different behavior for Ta-rich ( $x > 0.50$ ) and Ta-poor ( $x < 0.25$ ) conditions. In Fig. 5(a), the evolution of the cDOS of (TiZrHf)<sub>1-x</sub>Ta<sub>x</sub> alloys with Ta contents is displayed and compared to those of equimolar *hcp*-ZrHf, *bcc*-ZrTa and *bcc*-TiZrHf alloys.

Firstly, the stable *hcp*-ZrHf solid solution has a very narrow distribution of formation energies ( $\Delta E_f \sim 0$  meV/atom). In contrast, the unstable *bcc*-ZrTa solid solution has a very broad energy distribution at much higher  $\Delta E_f$  (50~200 meV/atom). Secondly, the  $\Delta E_f$  distribution of *bcc*-(TiZrHf)<sub>1-x</sub>Ta<sub>x</sub> alloys locates between the former two. At the same time, because of the expanding configuration space with the component numbers increasing, the cDOS peaks of *bcc*-(TiZrHf)<sub>1-x</sub>Ta<sub>x</sub> alloys remain much higher than those of the former mixtures with only two components. Thirdly, the cDOS peaks gradually grow higher with increasing configuration numbers when adding more Ta when  $x \leq 0.25$ . Furthermore, the  $\Delta E_f$  energy window progressively moves to higher  $\Delta E_f$ . After adding even more Ta ( $0.25 \leq x \leq 0.50$ ), the cDOS peaks grow shorter and broader with deflating configuration space. This is accompanied by their  $\Delta E_f$  values consistently climbing up. Upon further Ta addition, a sudden change of cDOS occurs for alloys at  $x = 0.66$  and  $0.75$ , where the energy window shrinks and moves down. One possible explanation for this is related to the stabilization of Ta-rich ( $x > 0.50$ ) *bcc* alloys resulting from the decrease of the internal energies as shown in Fig. 6(d).

Likewise, the deviation of the computed  $S_{\text{conf}}$  from the ideal-mixing limit, *i.e.*  $Q(T) = 1 - S_{\text{conf}}/S^{\text{id}}$  in Fig. 5(b), becomes more pronounced at higher Ta contents. This quantity measures the extent of chemistry heterogeneity for (TiZrHf)<sub>1-x</sub>Ta<sub>x</sub> alloys at various compositions. It is known that the stable *hcp*-ZrHf with  $Q(T)$  around 0 is the closest case to a random solid solution with chemistry homogeneity. In contrast, the unstable *bcc*-ZrTa with  $Q(T)$  around 1 at low temperatures is an example of mixtures with intensive chemistry heterogeneity and strong tendency towards phase separation after equilibrium processing or amorphization after non-equilibrium processing [39]. As displayed in Fig. 5(b), the  $Q(T)$  of all alloy systems is largely decreased at high temperatures, which is consistent with the suppressed demixing tendency at elevated temperatures. When adding Ta into (TiZrHf)<sub>1-x</sub>Ta<sub>x</sub>,  $Q(T)$  steadily increases until  $x = 0.66$ , then it decreases at  $x = 0.75$ . Therefore, the chemistry heterogeneity is enhanced with  $Q(T)$  increasing at high Ta contents. The only exception occurs for the Ta-rich corner at  $x = 0.75$ , which is a conventional solid solution with minor alloying



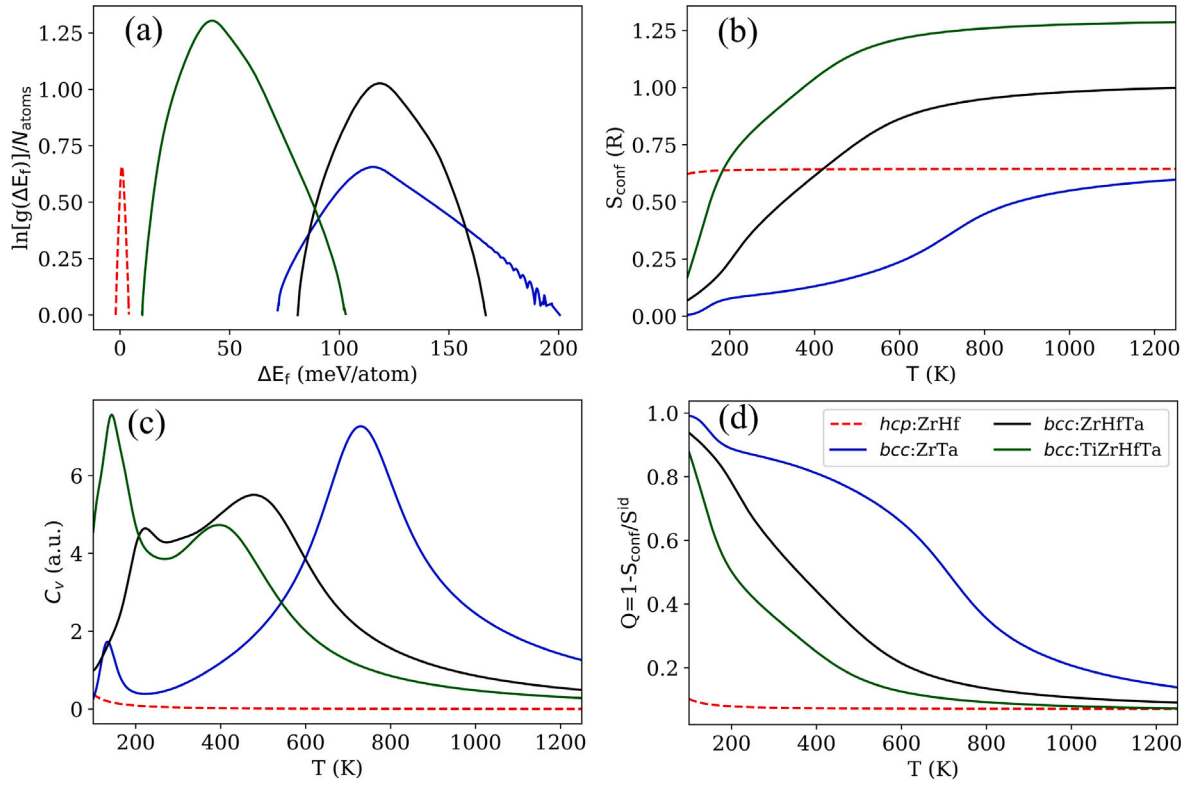


**Fig. 3.** Thermodynamical analysis of equiatomic *hcp* ZrHf, *bcc* ZrTa, *bcc* ZrHfTa and *bcc* TiZrHfTa, based on WL sampling and CE models. (a) configurational density of states normalized by the number of atoms ( $N_{\text{atoms}}$ ),  $\ln[g(\Delta E_f)]/N_{\text{atoms}}$ , (b) configurational entropy,  $S_{\text{conf}}$ , (c) configurational specific heat,  $C_v$ , and (d) degree of deviation of  $S_{\text{conf}}$  from the ideal mixing entropy,  $Q = 1 - S_{\text{conf}}/S^{\text{id}}$ . (For interpretation of the references to color in this figure legend, the reader is referred to the web version of this article.)

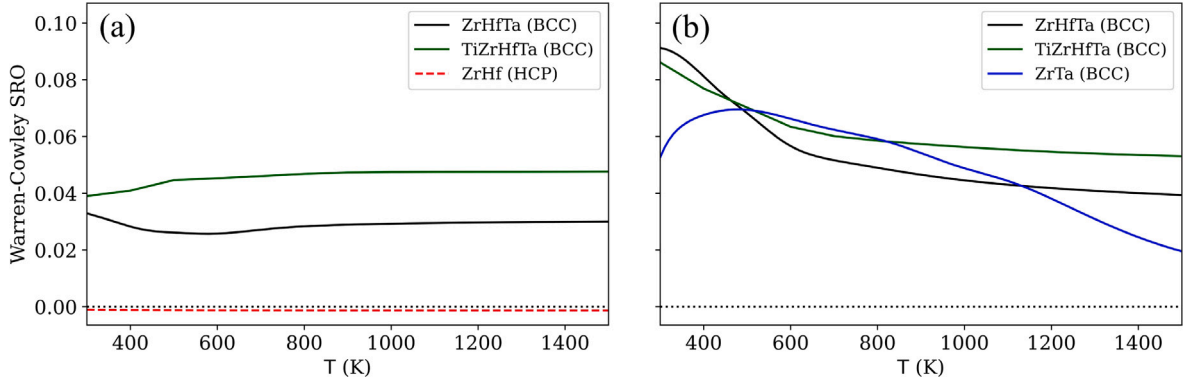


**Fig. 4.** Warren-Cowley short-range order (SRO) parameters as a function of temperature for the (a) Zr-Hf pairs and the (b) Zr-Ta pairs in equiatomic *hcp* ZrHf, *bcc* ZrTa, *bcc* ZrHfTa and *bcc* TiZrHfTa.

elements of Ti, Zr, Hf. Additionally, the  $Q(T)$  curves for  $x < 0.34$  are bowed down, which suggests the temperature range of demixing is very narrow. While those for  $x > 0.34$  are bowed up, which indicates a more broad temperature range of demixing as the case of unstable *bcc*-ZrTa.

Moving to the remaining thermodynamical quantities, we note that both the free energy,  $\Delta F_f$  in Fig. 6(a), and the internal energy,  $\Delta U_f$  in Fig. 6(d), increase linearly with the Ta content, at least at low and moderate temperatures. This is somehow expected considering the chemical dissimilarity between Ta and the other constituent elements, a feature that introduces a progressively large chemical heterogeneity.

At high temperature, 1600 K, the free energy in Fig. 6(a) presents a broad minimum plateau for  $x < 0.25$  and then increases approximately linearly. Such crossover concentration,  $x = 0.25$ , is associated to the stabilization of the equiatomic *bcc* TiZrHfTa alloy, where the computed

$S_{\text{conf}}$  is maximized [see Fig. 6(b)]. The large contribution of the configurational entropy to the *bcc*-stabilization at high temperature can also be appreciated by looking at the dimensionless parameter,  $\Omega = T S_{\text{conf}}/\Delta U_f$ , displayed in Fig. 6(c). Since HEAs are usually processed at high temperature, the *bcc* phase can be quenched down and trapped at low temperature due to sluggish diffusion effects. However, the drastic collapse of the configurational entropy at low temperature makes such *bcc* phase metastable. In fact, at low temperature the internal energy  $\Delta U_f$  completely dominates any entropic contribution to the Gibbs free energy. This means that the stability of the low-temperature phase is determined almost uniquely by the potential energy landscape, which, as investigated previously, suggests metastability. Furthermore, the  $\Delta U_f$  at 1600 K show a peak at  $x = 0.50$ . This is consistent with the broadening of the cDOS at higher formation energies in Fig. 5(a). It

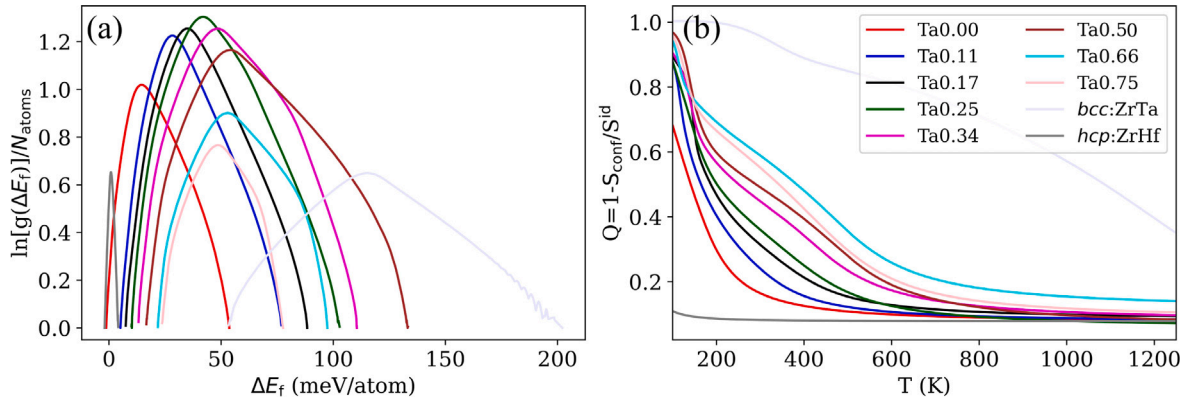


Fig. 5. Comparison of (a) cDOS and (b) the degree of deviation of  $S_{\text{conf}}$  from the ideal mixing entropy,  $Q = 1 - S_{\text{conf}}/S^{\text{id}}$ , at various compositions. Note that the cDOS is normalized by the number of atoms ( $N_{\text{atoms}}$ ) included in the simulation cells, namely we plot  $\ln[g(\Delta E_f)]/N_{\text{atoms}}$ .

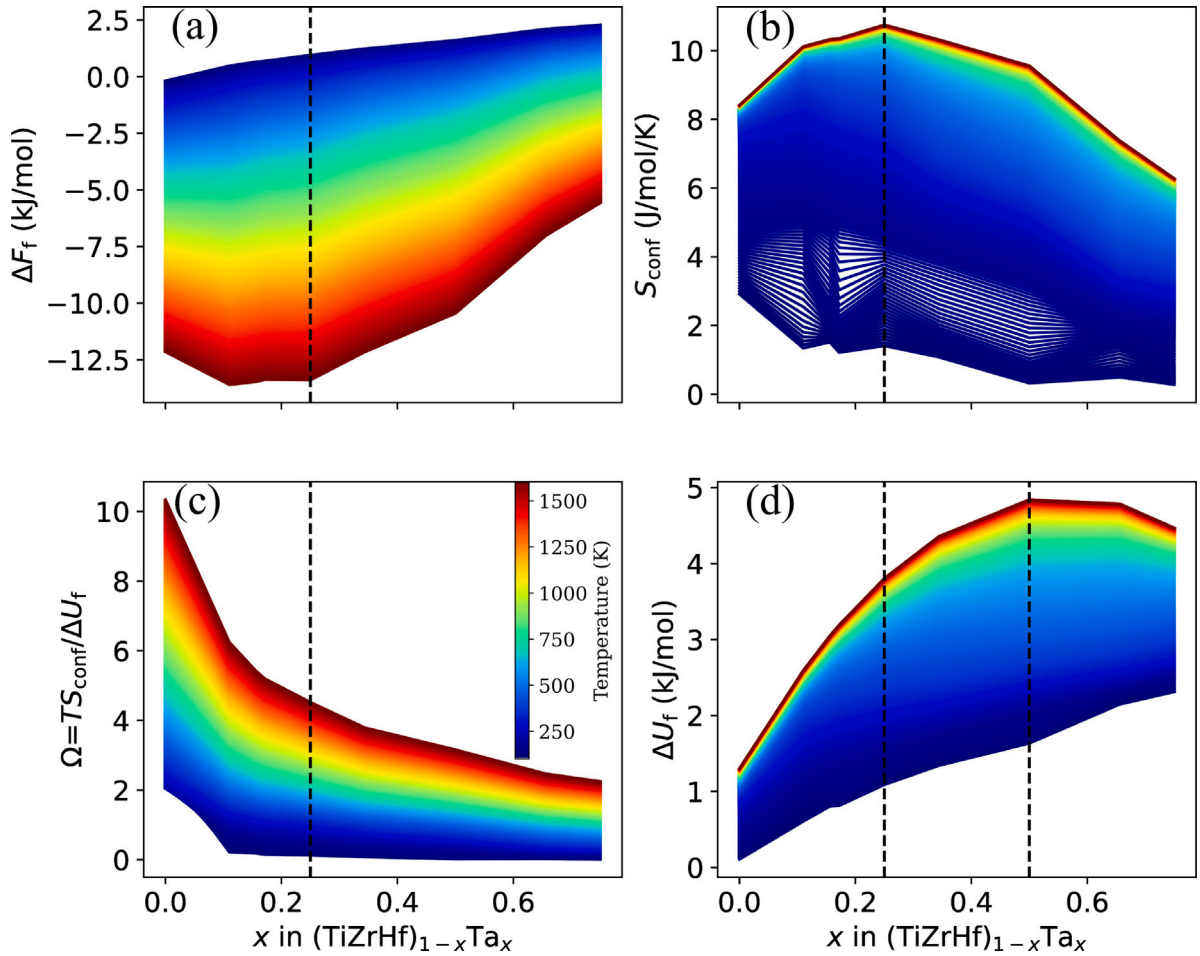


Fig. 6. Variation of (a) formation free energy ( $\Delta F_f$ , kJ/mol), (b) configurational entropy ( $S_{\text{conf}}$ , J/mol/K), (c)  $\Omega = TS_{\text{conf}}/\Delta U_f$  and (d) internal energy ( $\Delta U_f$ , kJ/mol) with Ta contents in  $\text{bcc}(\text{TiZrHf})_{1-x}\text{Ta}_x$ . The color from blue to red indicates the temperature variation from 100 to 1600 K (see color-code bar in panel (c)). (For interpretation of the references to color in this figure legend, the reader is referred to the web version of this article.)

suggests a maximization of destabilization, *i.e.* a strong tendency of demixing when adding 50% Ta into TiZrHf matrix.

#### 4. Discussion

In general, when entropic effects are important at high temperature,  $(\text{TiZrHf})_{1-x}\text{Ta}_x$  alloys behave as multi-component solid solutions

with relatively good mixability and low chemistry heterogeneity. However, when entropic effects are less important at low temperatures, we found  $(\text{TiZrHf})_{1-x}\text{Ta}_x$  alloys with low Ta contents to show some unique behaviors of glass materials: flexible structural transformation and complex microstructures due to high atomic activity hidden in shallow and flatten PEL, local chemistry heterogeneity and relatively wide energy distribution with a variety of energy states. Other glass-like behaviors have been also reported in metastable high-entropy



alloys with certain compositions, such as huge configuration space and long-range disorder [40], excellent defect-tolerance [41] and dynamic instability [42]. Furthermore, local chemistry heterogeneity is a significant microstructure feature of metastable HEAs at low and moderate temperatures. It is accompanied by relatively broad energy distribution and the variation of the local atomic structure stability. Local structural transitions or phase separations might be triggered during the equilibration processing, and there is even a chance of glass transition if non-equilibrium processing is applied. This makes the modeling and the microstructure study of metastable high-entropy alloys much more complex. Although one single SQS cell is feasible for modeling random solid solution at high temperatures, delicate techniques are required to extract the variation of the energy distribution accompanying the local chemistry heterogeneity. In this work, the structure enumeration, together with the combination of WL with CE techniques provide new perspectives into the metastability exploration in multicomponent systems with significant chemistry heterogeneity. As a final comment we note that the exact thermodynamic conditions, leading to the structural transformation between the *bcc* and *hcp* phase, can only be accurately computed by considering the effects of the configuration heterogeneity over the lattice vibrations for both structures. This will be addressed in a future work.

## 5. Conclusions

In contrast to single-phase random solid-state solutions, which typically present a homogeneous structure, metastable HEAs are characterized by composition fluctuations and disturbance of the homogeneity of the chemical interaction at low temperature. This is analyzed here for the Ti–Zr–Hf–Ta system as a function of the Ta content. The fingerprints of the metastability are found in the evolution of the meta-basins in the potential energy landscape, the wide energy window of configurations available to the system, the large deviation of  $S_{\text{conf}}$  from  $S^{\text{id}}$  and the evolution of short-range order parameters with the Ta content. One can then conclude that the shallow potential energy landscape of metastable HEAs occupies a large hyper-volume of the configuration space, which may incorporate indispensable fluctuations in the local chemistry and configurations. In this situation flexible atomic-structure tuning, such as martensitic transformations and local ordering, can be triggered when applying an external mechanical and/or thermal load. Such collection of features of metastable HEAs bears a certain similarity with those of metallic glasses. Most importantly, such description holds true for metastable HEAs at low and cryogenic temperatures. In contrast, at elevated temperatures, where  $S_{\text{conf}}$  is close to  $S^{\text{id}}$ , their stability is entropically enhanced and behavior similar like solid solution dominates.

A more precise evaluation of the thermodynamical conditions leading to the various possible structural transformations, require the description of kinetic and dynamic properties, in addition to the study of the configuration space and thermodynamic properties. This is a challenging theoretical task, which nevertheless may shade light onto the microscopic drive to metastability. Such issue will be addressed in future work. In conclusion, by exploring the energetic and configurational space of the metastable Ti–Zr–Hf–Ta system, we have obtained insights into the glass-like characters of metastable HEAs at low temperatures, suggesting a new interpretative key for understanding the underlying mechanisms behind the formation of distinct metastable states in HEAs.

## Declaration of competing interest

The authors declare that they have no known competing financial interests or personal relationships that could have appeared to influence the work reported in this paper.

## Acknowledgments

YH would like to acknowledge the financial support from the Natural Science Foundation of China (No. 52102079), the Hundred Talents Program of Hubei Province (No. E2020050017) and the Innovation Ability Promotion Project of Hebei (No. 22567609H) supported by Hebei key lab for optimizing metal product technology and performance. YK gets supports from the internal grant of Hebei Normal University of Science & Technology Research Program (No. 2021jk10). SS thanks the Irish Research Council, Ireland for financial support through the Advanced Laureate Award (IRCLA/2019/127). Computational resources have been provided by the Trinity Centre for High Performance Computing (TCHPC) and the TianHe-2A system of the National Supercomputer Center in Guangzhou (NSCC-GZ), China. LM gets financial support from the Natural Science Foundation of China (No. 52271155) and the National Key R&D Program of China (No. 2018YFA0703602).

## Appendix A. Supplementary data

Supplementary material related to this article can be found online at <https://doi.org/10.1016/j.actamat.2023.119031>.

## References

- [1] J.W. Yeh, S.K. Chen, S.J. Lin, J.Y. Gan, T.S. Chin, T.T. Shun, C.H. Tsau, S.Y. Chang, Nanostructured high-entropy alloys with multiple principal elements: Novel alloy design concepts and outcomes, *Adv. Eng. Mater.* 6 (2004) 299–303.
- [2] R. Feng, P.K. Liaw, M.C. Gao, M. Widom, First-principles prediction of high-entropy-alloy stability, *npj Comput. Mater.* 3 (2017) 1–6.
- [3] E.P. George, D. Raabe, R.O. Ritchie, High-entropy alloys, *Nat. Rev. Mater.* 4 (2019) 515–534.
- [4] Z. Li, K.G. Pradeep, Y. Deng, D. Raabe, C.C. Tasan, Metastable high-entropy dual-phase alloys overcome the strength-ductility trade-off, *Nature* 534 (2016) 227–230.
- [5] T. Yang, Y.L. Zhao, Y. Tong, Z.B. Jiao, J. Wei, J.X. Cai, X.D. Han, D. Chen, A. Hu, J.J. Kai, K. Lu, Y. Liu, C.T. Liu, Multicomponent intermetallic nanoparticles and superb mechanical behaviors of complex alloys, *Science* 362 (2018) 933–937.
- [6] P. Wang, Y. Bu, J. Liu, Q. Li, H. Wang, W. Yang, Atomic deformation mechanism and interface toughening in metastable high entropy alloy, *Mater. Today* 37 (2020) 64–73.
- [7] H. Huang, Y. Wu, J. He, H. Wang, X. Liu, K. An, W. Wu, Z. Lu, Phase-transformation ductilization of brittle high-entropy alloys via metastability engineering, *Adv. Mater.* 29 (2017) 1–7.
- [8] Q. Ding, X. Fu, D. Chen, H. Bei, B. Gludovatz, J. Li, Z. Zhang, E.P. George, Q. Yu, T. Zhu, R.O. Ritchie, Real-time nanoscale observation of deformation mechanisms in CrCoNi-based medium- to high-entropy alloys at cryogenic temperatures, *Mater. Today* 25 (2019) 21–27.
- [9] B. Gludovatz, A. Hohenwarter, D. Catoor, E.H. Chang, E.P. George, R.O. Ritchie, A fracture-resistant high-entropy alloy for cryogenic applications, *Science* 345 (2014) 1153–1158.
- [10] B. Gludovatz, A. Hohenwarter, K.V. Thurston, H. Bei, Z. Wu, E.P. George, R.O. Ritchie, Exceptional damage-tolerance of a medium-entropy alloy CrCoNi at cryogenic temperatures, *Nature Commun.* 7 (2016) 1–8.
- [11] S. Wang, M. Wu, D. Shu, G. Zhu, D. Wang, B. Sun, Mechanical instability and tensile properties of TiZrHfNbTa high entropy alloy at cryogenic temperatures, *Acta Mater.* 201 (2020) 517–527.
- [12] J. Rackwitz, Q. Yu, Y. Yang, G. Laplanche, E.P. George, A.M. Minor, R.O. Ritchie, Effects of cryogenic temperature and grain size on fatigue-crack propagation in the medium-entropy CrCoNi alloy, *Acta Mater.* 200 (2020) 351–365.
- [13] B. Chen, S. Li, H. Zong, X. Ding, J. Sun, E. Ma, Unusual activated processes controlling dislocation motion in body-centered-cubic high-entropy alloys, *Proc. Natl. Acad. Sci. USA* 117 (2020) 16199–16206.
- [14] Y. Zhang, G.M. Stocks, K. Jin, C. Lu, H. Bei, B.C. Sales, L. Wang, L.K. Béand, R.E. Stoller, G.D. Samolyuk, M. Caro, A. Caro, W.J. Weber, Influence of chemical disorder on energy dissipation and defect evolution in concentrated solid solution alloys, *Nature Commun.* 6 (2015).
- [15] Y.H. Zhang, Y. Zhuang, A. Hu, J.J. Kai, C.T. Liu, The origin of negative stacking fault energies and nano-twin formation in face-centered cubic high entropy alloys, *Scr. Mater.* 130 (2017) 96–99.
- [16] J. Ding, Q. Yu, M. Asta, R.O. Ritchie, Tunable stacking fault energies by tailoring local chemical order in CrCoNi medium-entropy alloys, *Proc. Natl. Acad. Sci. USA* 115 (2018) 8919–8924.
- [17] C.M. Rost, E. Sachet, T. Borman, A. Moballeghe, E.C. Dickey, D. Hou, J.L. Jones, S. Curtarolo, J.P. Maria, Entropy-stabilized oxides, *Nature Commun.* 6 (2015).

- [18] S. Curtarolo, W. Setyawan, G.L.W. Hart, M. Jahnatek, R.V. Chepulskii, R.H. Taylor, S. Wang, J. Xue, K. Yang, O. Levy, M.J. Mehl, H.T. Stokes, D.O. Demchenko, D. Morgan, AFLOW: An automatic framework for high-throughput materials discovery, *Comput. Mater. Sci.* 58 (2012) 218–226.
- [19] C. Toher, C. Oses, D. Hicks, S. Curtarolo, Unavoidable disorder and entropy in multi-component systems, *npj Comput. Mater.* 5 (2019) 10–12.
- [20] P. Sarker, T. Harrington, C. Toher, C. Oses, M. Samiee, J.P. Maria, D.W. Brenner, K.S. Vecchio, S. Curtarolo, High-entropy high-hardness metal carbides discovered by entropy descriptors, *Nature Commun.* 9 (2018) 1–10.
- [21] A. Fernández-Caballero, M. Fedorov, J.S. Wróbel, P.M. Mummery, D. Nguyen-Manh, Configurational entropy in multicomponent alloys: Matrix formulation from ab initio based hamiltonian and application to the FCC Cr-Fe-Mn-Ni system, *Entropy* 21 (2019).
- [22] C.M. Nataraj, A. van de Walle, A. Samanta, Temperature-dependent configurational entropy calculations for refractory high-entropy alloys, *J. Phase Equilibria Diffus.* (2021).
- [23] J. Wang, J. Li, Q. Wang, J. Wang, Z. Wang, C.T. Liu, The incredible excess entropy in high entropy alloys, *Scr. Mater.* 168 (2019) 19–22.
- [24] M. Ångqvist, W.A. Muñoz, J.M. Rahm, E. Fransson, C. Durniak, P. Rozyczko, T.H. Rod, P. Erhart, ICET – A Python library for constructing and sampling alloy cluster expansions, *Adv. Theory Simul.* 1900015 (2019) 1900015.
- [25] A. van de Walle, P. Tiwary, M. de Jong, D.L. Olmsted, M. Asta, A. Dick, D. Shin, Y. Wang, L.Q. Chen, Z.K. Liu, Efficient stochastic generation of special quasirandom structures, *CALPHAD* 42 (2013) 13–18.
- [26] G.L.W. Hart, R.W. Forcade, Algorithm for generating derivative structures, *Phys. Rev. B* 77 (2008) 224115.
- [27] F. Wang, D.P. Landau, Efficient, multiple-range random walk algorithm to calculate the density of states, *Phys. Rev. Lett.* 86 (2001) 2050–2053.
- [28] G. Kresse, D. Joubert, From ultrasoft pseudopotentials to the projector augmented-wave method, *Phys. Rev. B* 59 (1999) 1758–1775.
- [29] A. Seko, Y. Koyama, I. Tanaka, Cluster expansion method for multicomponent systems based on optimal selection of structures for density-functional theory calculations, *Phys. Rev. B* 90 (2009) 165122.
- [30] Y. Zhang, B. Liu, J. Wang, Self-assembly of Carbon Vacancies in Substoichiometric ZrCl<sub>x</sub>, *Sci. Rep.* (2015) accepted.
- [31] P.E. Blöchl, Projector augmented-wave method, *Phys. Rev. B* 50 (1994) 17953–17979.
- [32] J.P. Perdew, K. Burke, M. Ernzerhof, Generalized gradient approximation made simple, *Phys. Rev. Lett.* 77 (1996) 3865–3868.
- [33] D. Machon, F. Meersman, M.C. Wilding, M. Wilson, P.F. McMillan, Pressure-induced amorphization and polyamorphism: Inorganic and biochemical systems, *Prog. Mater. Sci.* 61 (2014) 216–282.
- [34] Z.M. Wong, T.L. Tan, S.W. Yang, G.Q. Xu, Optimizing special quasirandom structure (SQS) models for accurate functional property prediction in disordered 2D alloys, *J. Phys. Condens. Matter* 30 (2018).
- [35] C. Wolverton, A. Zunger, Ising-like description of structurally relaxed ordered and disordered alloys, *Phys. Rev. Lett.* 75 (1995) 3162–3165.
- [36] Q.F. He, P.H. Tang, H.A. Chen, S. Lan, J.G. Wang, J.H. Luan, M. Du, Y. Liu, C.T. Liu, C.W. Pao, Y. Yang, Understanding chemical short-range ordering/demixing coupled with lattice distortion in solid solution high entropy alloys, *Acta Mater.* 216 (2021) 117140.
- [37] Z. Pei, R. Li, M.C. Gao, G.M. Stocks, Statistics of the NiCoCr medium-entropy alloy: Novel aspects of an old puzzle, *npj Comput. Mater.* 6 (2020).
- [38] J.M. Cowley, An approximate theory of order in alloys, *Phys. Rev.* 77 (1950) 669–675.
- [39] A.B. Behboud, A. Motallebzadeh, S. Öner, Nanoheterogeneous ZrTa metallic glass thin films with high strength and toughness, *J. Alloys Compd.* 901 (2022) 163578.
- [40] J. Zhang, C. Cai, G. Kim, Y. Wang, W. Chen, Composition design of high-entropy alloys with deep sets learning, *npj Comput. Mater.* 8 (2022) 1–11.
- [41] P. Agrawal, R.S. Haridas, S. Thapliyal, S. Yadav, R.S. Mishra, B.A. McWilliams, K.C. Cho, Metastable high entropy alloys: An excellent defect tolerant material for additive manufacturing, *Mater. Sci. Eng. A* 826 (2021) 142005.
- [42] K. Gubaev, Y. Ikeda, F. Tasnáí, J. Neugebauer, A.V. Shapeev, B. Grabowski, F. Körmann, Finite-temperature interplay of structural stability, chemical complexity, and elastic properties of bcc multicomponent alloys from ab initio trained machine-learning potentials, *Phys. Rev. Mater.* 5 (2021) 1–10.